Position Accuracy of a 6-DOF Passive Robotic Arm for Ultrasonography Training

Tanmine Mesatien
International School of Engineering
Chulalongkorn University
Bangkok, Thailand

Ravicha Suksawasdi Na Ayuthaya
International School of Engineering
Chulalongkorn University
Bangkok, Thailand

Apirat Chenviteesook
International School of Engineering
Chulalongkorn University
Bangkok, Thailand

Ronnapee Chaichaowarat *
International School of Engineering
Chulalongkorn University
Bangkok, Thailand
ronnapee.c@chula.ac.th

***Abstract*—Image processing was applied for the real-time evaluation of ultrasound imaging quality. Simultaneous observation of the ultrasound probe's contacting force, tilting orientation, and operational trajectory in spatial coordinates can provide useful feedback for supporting ultrasonography training. This paper presents a 6-DOF passive robotic arm enabling the complete tracking of the probe position and orientation. The custom designed handle located at the end effector is assembled from the inner and outer shells, which allows installation of a tiny three-axis force sensor for measuring the probe contact force. The forward kinematics of the robot arm is derived for mapping the joint variables to the position and orientation of the tip. The real-time measurement of the joint angles is achieved from the non-contact magnetic encoders for the first to fourth revolute joints and the rotary potentiometers for the 2-DOF ball joint. The three-dimensional testbed consisting of the radial arrays of hexagonal slots is used for evaluating the position and orientation accuracy of the passive arm. The results of this study can be used as a guideline for further development of passive robotic arms to achieve a higher level of accuracy on tracking the probe trajectory.**

Keywords—Passive manipulator, ultrasound robot, forward kinematics

I. INTRODUCTION

Ultrasound imaging of the abdomen is a convenient and painless method to obtain visual representation of abdominal organs for scanning diseases and abnormalities. The real-time imaging with high spatial resolution can be achieved by this non-invasive method. The technique is low cost and low risk of ionizing radiation as compared with other medical imaging techniques such as computed tomography (CT), magnetic resonance imaging (MRI), and positron emission tomography (PET). Since the conventional ultrasound only displays two-dimensional image covering the region of interest, the effective use of ultrasound strongly requires an understanding, combined with the ability to interpret the sonographic images. Artificial intelligence was applied to aid detecting abnormalities for real-time ultrasound [1].

Observing medical professionals of different experience levels while performing ultrasound scans to provide adequate feedback is very important for training and improving their skills. The inertial measurement unit was applied for capturing the acceleration and angular velocity of the ultrasound probe to provide real-time feedback to medical students during training [2]. The scanning trials performed by novices and experts show the speed variation among them while scanning different organs. However, the probe contact force measurement and the trajectory in spatial coordinates were not mentioned in the study. Aligning the probe axis normal to the anatomical surface at the contact point is required for good image quality in orthopedic ultrasound. The automatic normal positioning for 3D alignment of the probe axis [3] was achieved based on confidence map optimization [4] and force measurement, without using additional sensors for surface reconstruction or localizing the point of contact. The ultrasound image was used for inspecting the length of muscle thickness in the thigh to detect Sarcopenia [5]. The angular surface of the human thigh was curved fitted based on the depth measurement of an RGB-depth camera in order to use as the reference trajectory for moving the ultrasound probe angularly along the convex surface of the thigh with predefined pressure. The probe-camera system was proposed for 3D ultrasound image reconstruction [6]. The volumetric ultrasound image is acquired by sweeping the probe around the area of interests to integrate a set of 2D images. The freehand protocol is cost-effective and flexible. The accurate position of the ultrasound probe can be obtained from the electromagnetic devices [7]. The 3D image can be obtained from a 2D probe without initial marks with the low-cost handheld system [8] consisting of three ultrasonic distance sensors installed perpendicular to each other, a gimble, and an IMU sensor. The error of position estimation was evaluated through the XYZ stage setup. The calibration phantom combined with the tracking stylus was proposed [9] for accurately determining the spatial position difference between the B-scan image and the probe tracked by the position tracking device. The probe was attached by the marker frame of optical spears and needle. The phantom was designed for the placement of needle and stylus. The co-planar relationship between their tips was considered for calibration.

We have proposed an affordable technique for observing the position and orientation of the ultrasound probe by using an RGB-depth camera [10]. By applying the MediaPipe Hands framework [11] [12] for tracking the hand gesture, no additional marker (which can interfere with the motion) is required on the handheld probe. However, the accuracy of the method is limited. The passive articulated arm provides accurate results for coordinate measuring machines [13]. As an alternative strategy, this paper presents a 6-DOF passive robotic arm for the complete tracking of the probe position and orientation. The custom designed handle located at the

The first, second, and third authors contributed equally to this work.

end effector is assembled from the inner and outer shells, which allows installation of a tiny three-axis force sensor for measuring the probe contact force. The forward kinematics of the robot arm is derived for mapping the joint variables to the position and orientation of the tip. The position and orientation accuracy of the passive arm was evaluated experimentally using a three-dimensional testbed consisting of radial arrays of hexagonal slots.

This paper is organized as follows: Section II introduces the design and hardware integration of the passive robotic arm and the custom probe handle. Section III derives the forward kinematics. Section IV describes the experimental setup. Section V discusses the results and Section VI summarizes the key findings.

II. Design and Hardware Integration

A. The 6-DOF Passive Robotic Arm

The determination of the end-effector position and orientation in a 6-degree-of-freedom (DOF) passive robotic arm, as shown in Fig. 1, relies on the measurement of six joint displacements. In this section, we describe the methods used to measure these joint displacements, specifically focusing on joints $j_1 - j_4$, which are measured using TLE5012b magnetic rotary encoders, and joints $j_5 - j_6$, which are measured using analog potentiometers.

Joints $j_1 - j_4$ are equipped with TLE5012b magnetic rotary encoders, where an aluminum shaft is attached to these revolute joints. The rotation of the aluminum shaft induces changes in the magnetic field, resulting in variations in the electrical resistance of the encoder sensor. By accurately measuring these changes in resistance, the corresponding angle information can be calculated, thereby determining the joint displacements.

To comply with the last two degrees of freedom of the ball joint, the two analog potentiometers are used for the joints $j_5 - j_6$. The potentiometer consists of a resistive element and a wiper that moves along it as the shaft rotates. As the wiper position changes, the resistance between the wiper and the other two terminals of the potentiometer also varies. Consequently, this change in resistance leads to a corresponding change in voltage at the wiper. To establish a reliable relationship between the analog voltage value and the angle of rotation, a calibration curve or equation is developed by rotating the shaft through a full 360-degree range. This calibration process enables accurate conversion of the analog voltage readings to the corresponding joint angles.

B. Ultrasound Probe Handle

To ensure the experimental setup closely resembled real-world conditions, it was necessary to design the ultrasound probe model with utmost accuracy. The 3D scanned model of the actual probe, as shown in Fig. 2(a), was utilized as a reference in this study. One of the key design modifications focused on the tip of the ultrasound probe. To facilitate the experimental procedures, a hexagonal shaft with a diameter of 9.8 mm was incorporated into the design of the 3D printed ultrasound probe, as shown in Fig. 2(b).

The custom designed handle enabling the probe contact force measurement is shown in Fig. 3. The handle consists of the 3D printed inner and outer shells. The design is easy to assemble with the ultrasound probe without requiring any

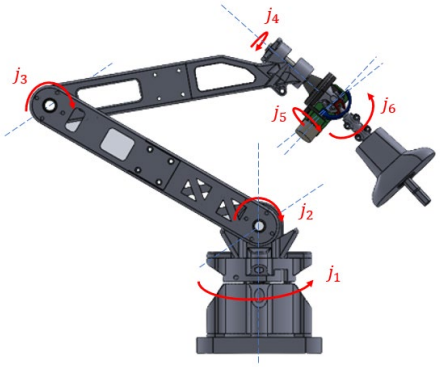

Fig. 1. CAD redering shows the six revolute joints of the 6-DOF passive robotic arm.

(a) (b)

Fig. 2. (a) 3D scanned model of the ultrasound probe. (b) The 3D printed ultrasound probe with hexagonal shaft at the tip is used for the experiment.

Fig. 3. The custom handle enabling the probe contact force measurement is designed to closely resemble the shape of the original ultrasound probe. The Tec Gihan's USL06-H5 three-axis force sensor is installed on the outer shell. The cover of the inner shell is mounted on the top surface of the force sensor. The ultrasound probe is placed inside the inner shell. The force sensor is the single-point contact between the shells designed with adequate clearance for the accurate force measurement.

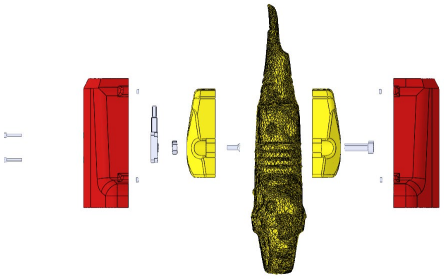

Fig. 4. The model of the probe is obtained from the 3D scanning process. The inner shell is assembled from the two casing parts (yellow). The outer shell consists of two parts (red) attached to each other by the neodymium magnets. The force sensor is located between the inner and outer shells.

modification. See Fig. 4, the inner shell is assembled from the two casing parts (shown in yellow) for accommodating the probe. The 3D model of the probe with complex surface is obtained from the 3D scanning process. The outer shell specially designed for installation of the Tec Gihan's USL06-H5 three-axis force sensor consists of two parts (shown in red). The handle design closely resembles the shape of the original ultrasound probe to minimize disruptions to the sonographer's examination technique. The interaction force between the probe and the human body is directly transferred to the inner shell. The force sensor located between the inner and outer shells provides the single-point contact between them to make sure the probe contact force is read accurately. For convenient disassembly, the two parts of the outer shell are firmly attached with each other by the implanted eight high-strength neodymium magnets (creating force of 5 N). The clearance between the outer and inner shells is not less than 5.0 mm to prevent the shell-to-shell movement in the X and Y directions, while the force sensor prevents the motion along the Z direction. The force sensor is fastened to the outer shell with the use of four M2 hex socket head cap screws, while the M3 Phillips pan head screw is utilized to fasten one piece of the inner shell to the force sensor. Both pieces of the inner shell are assembled with each other by M4 hex socket head cap screws.

C. *Hardware Configuration*

Diagram in Fig. 5 shows the hardware setup in our study. The robotic arm joint angles are dictated by the three-dimensional testbed. Then, Arduino continuously reads encoders and potentiometers values from the robotic arm, see Fig. 6, and calculates angles based on potentiometers and encoders readings and sends the time-varying angles to the computer. MATLAB's role is to establishes a connection with the Arduino through the serial port and receives data from it. The received data corresponds to angles measured by sensors attached to a robotic arm. Then, the code defines the Denavit-Hartenberg (DH) parameters, which describe the geometry and kinematics of the robot. The angles are used to calculate the forward kinematics, by obtaining the product of the transformation matrices of all the joints.

The position vector describing X, Y, and Z coordinates of the ultrasound probe's tip can be obtained from the transformation matrix relating the end effector to the base frame for displaying the tip's position on the X-Y plane and the X-Z plane in real time. The rotation about X-Y-Z axes can also be derived from the rotation matrix obtained from the homogeneous transform. For the ultrasound application, the Euler angles about the three axes fixed to the handle is required for describing the rotation about the axis normal to the plane of contact and the tilting angles measured about the other two axes creating the plane of contact.

III. Forward Kinematics

A. *Obtaining the Denavit–Hartenberg Parameters*

In robotics, the DH notation is a widely used method for describing the kinematics of robotic arms. One key aspect of the DH notation is defining the attachment of link frames along the robot's arm. This involves assigning coordinate frames to each joint and link in a systematic manner. The link-frame attachment of the 6-DOF passive robotic arm is shown in Fig. 7.

The DH notation provides a set of parameters for each link-frame attachment, including the link length, link twist,

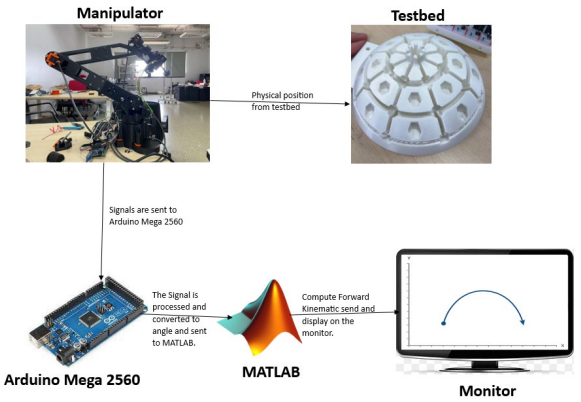

Fig. 5. Hardware setup. Arduino is used to acquire the encorder and potentiometer measurements from the passive robotic arm and transder the data for MATLAB calculation and display.

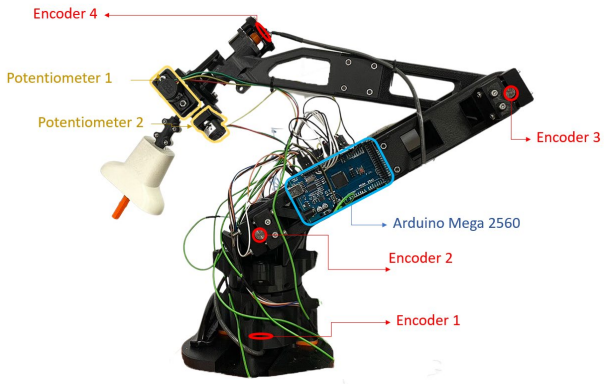

Fig. 6. Encoders and potentiometers are used for measuring the joint angles of the 6-DOF passive robotic arm.

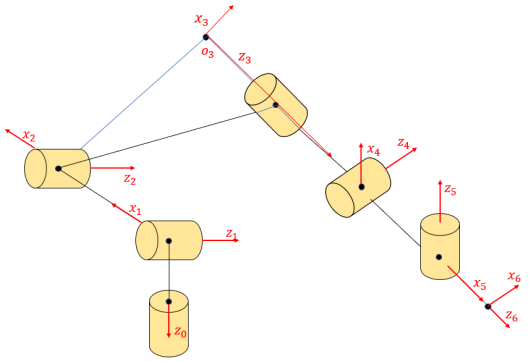

Fig. 7. Link-frame attachment of the 6-DOF passive robotic arm.

link offset, and joint angle. These parameters are used to construct transformation matrices that represent the relative pose between adjacent frames.

Starting from the base of the robot, each link's frame is attached to its corresponding joint, and the parameters are determined according to the DH convention. The link length represents the distance along the joint's axis from the previous frame to the current joint. The link twist denotes the rotation about the previous frame's z-axis required to align with the current joint's z-axis. The link offset accounts for the displacement along the previous frame's z-axis to reach the current joint's z-axis. Finally, the joint angle represents the rotation about the current joint's z-axis. The DH parameters of the 6-DOF passive robotic arm (including the end-effector mapping offset) are shown in Table I. The values are obtained through the measurement from CAD.

TABLE I. DH PARAMETERS OF THE 6-DOF PASSIVE ROBOTIC ARM

Joint	Link Length (a) (mm)	Link Twist (α) (degree)	Link Offset (d) (mm)	Joint Angle (Θ) (degree)
1	0	-90	0	Θ1*
2	300	0	0	Θ2* + 30
3	230	-90	0	101.3 – Θ3*
4	0	90	262	Θ4*
5	0	90	0	90+ Θ5*
6	0	90	0	90+ Θ6*
7	0	0	12	0

Note: the "*" symbol indicates the joint variables measured by sensors.

By defining the link-frame attachments using the DH notation, it becomes possible to establish the kinematic relationships between the joints and accurately determine the position and orientation of the robot's end effector in relation to its base.

B. Forward Kinematics and Trajectory

DH-Parameters is used for further calculation of forward kinematic. The homogeneous transform matrix (1) from the base link to the end effector is a special matrix which describes how the end effector of the robot is related to the home position. It combines all the individual transformations of each part of the robot's arm to give us the overall position and orientation of the end effector.

$$T = \begin{pmatrix} R & p \\ o & 1 \end{pmatrix} = \begin{pmatrix} r_{11} & r_{12} & r_{13} & p_1 \\ r_{21} & r_{22} & r_{23} & p_2 \\ r_{31} & r_{32} & r_{33} & p_3 \\ 0 & 0 & 0 & 1 \end{pmatrix} \quad (1)$$

Rotational Matrix — positional Matrix

To obtain the homogeneous transform, the transformation matrices of each link-frame attachment are successively multiplied together, starting from the base link and moving towards the end effector. This composition of transformations combines the translation and rotation information of each frame to generate a single matrix that describes the overall transformation.

$${}^{0}_{e}T = {}^{0}_{1}T\,{}^{1}_{2}T\,{}^{2}_{3}T\,{}^{3}_{4}T\,{}^{4}_{5}T\,{}^{5}_{6}T\,{}^{6}_{e}T \quad (2)$$

After setting the parameter and environment. the forward kinematic is calculated by MATLAB. Starting by getting the angle data from an Arduino board. Then, input the data into DH-Parameters. The DH-Parameter metrics are then used to compute the position of the end-effector and plot on the set figures. Then, after the forward kinematics is calculated the positional data (P_x, P_y, P_z) can be directly used by getting the data from obtaining the accessing the (1,4), (2,4), and (3,4) respectively from the homogeneous transform relating the base to the end effector.

The rotation about the X-Y-Z axes can be derived from the rotation matrix through the homogeneous transform. The order in which the rotations are applied can be different, such as XYZ, ZYX, or YZX, and the order of rotation we used are ZYX. Once, the rotation matrix of ZYX is found, then the rotation matrix about ZYX can be compared with rotation matrix of the homogenous transform. Then, the angles about the global X-axis, Y-axis, and Z-axis are obtained for describing the orientation of the end effector.

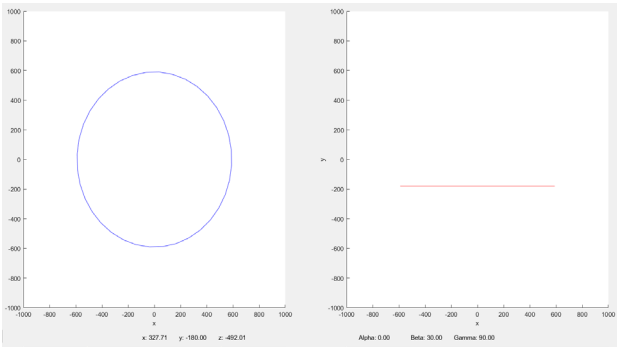

Fig. 8. Graphic user interface shows the real-time plot of the end-effector position on the X-Z and the X-Y planes.

$$R_x = atan2(end\_eff[3,2],\ end\_eff[3,3]) \quad (3)$$

$$R_y = atan2\left(-end\_eff[3,2],\ \sqrt{end\_eff[1,1]^2 + end\_eff[2,1]^2}\right) \quad (4)$$

$$R_z = atan2(end\_eff[2,1],\ end\_eff[1,1])] \quad (5)$$

Upon obtaining the measurements for position and orientation, it is possible to generate a real-time plot that serves as a graphical user interface (GUI) for user feedback. This interactive display, as shown in Fig. 8, enhances the user experience by providing a visual representation of the robotic arm's current position and orientation. The display includes the positional graph of a X-Z plane, X-Y plane, and numerical data of an orientation.

IV. EXPERIMENTAL SETUP

A. Three-dimensional Testbed

In order to assess the precision and accuracy of a measurement system designed to capture both linear displacements (P_x, P_y, P_z) and rotational displacements (R_x, R_y, R_z), a custom test plate was designed, as shown in Fig. 9. The test plate was specifically designed to replicate the abdominal region of an average adult human, providing a realistic and controlled environment for experimental evaluation.

The test plate features a diameter of 140mm and comprises a combination of 17 flat hexagonal slots and 16 inclined hexagonal slots. These slots were strategically arranged to mimic the anatomical complexity of the abdominal region. By incorporating both flat and inclined slots, the test plate allows for a comprehensive assessment of the measurement system's capabilities in capturing various surface geometries.

To introduce variations in height and test the system's detection power, the test plate incorporates three levels of slot height. The first and second levels exhibit a 7mm difference along the Z-axis, while a larger 17mm difference exists between the second and third levels. This design feature enables the investigation of how different magnitudes of height differences impact the precision and accuracy of the measurement system.

The selection of hexagonal slots serves a specific purpose in this study. The aim is to determine whether the measured

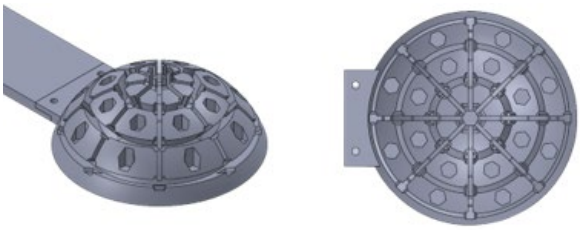

Fig. 9. 3D Design of the experimental testbed.

rotational displacements accurately correspond to the actual rotational displacements, where each edge-to-edge rotation is precisely 60 degrees. This design choice allows for a focused evaluation of the system's ability to capture and measure rotational movements with high accuracy.

B. *Experimental Method*

There are two sections dedicated to testing the precision and accuracy of the robotic arm, which are position and orientation testing. Each section consists of five trials, and the results obtained from these trials are utilized in the subsequent analysis and discussion.

The first test focuses on position verification. The testing order follows a specific sequence: 0, 11, 12, 0, 21, 22, ..., 0, 81, 82, as illustrated in Fig. 10. Consequently, there are 24 points evaluated per trial. The recorded results are then compared with the actual positions to calculate the errors.

The orientation test comprises of three subsections, as each axis's rotational angle is measured independently. Notably, it is essential to strictly follow to the Euler angle convention to ensure accurate orientation values. Therefore, the testing procedure must begin by rotating along the Z-axis, followed by the Y-axis, and finally, the X-axis. For Z-axis measurement, the probe is inserted into the top hole (point 0) as illustrated in Fig. 10, Subsequently, the probe is removed, rotated 60 degrees, and reinserted into the hole, with this process repeated six times per trial.

For Y-axis measurement, the testing point is indicated in blue as depicted in Fig. 11. The procedure begins rotating the Z-axis of the arm by 45 degrees; therefore, it obeys the Euler angle convention. Then, the recording process begins by inserting the probe into the top hole (point 0) and subsequently moving to the highlighted hole on the negative X side of the testbed. The probe then returns to point 0 and proceeds to the positive X side.

For angle of rotation about the X-axis. The procedure begins by inserting the probe into the top hole. The testing point is identified and marked in red, as illustrated in Fig. 11. Subsequently, the probe is directed towards the highlighted hole located on the negative X side of the testbed, then the probe is returned to Point 0, and then it proceeds to the positive x side of the testbed.

V. Experimental Results

The average differences and standard deviations were calculated to assess accuracy and precision.

A. *Position Accuracy*

The position accuracy is shown in Fig. 12 and summarized in Table II. The position error is most significant in the X-axis, followed by the Y-axis, while the Z-axis demonstrates higher accuracy. The reason behind the significance error is the miscounting of encoder. From

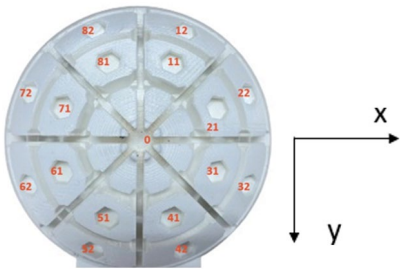

Fig. 10. Labeled testbed describing the position accuracy test.

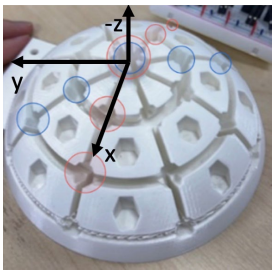

Fig. 11. Labeled testbed describing the orientation accuracy test.

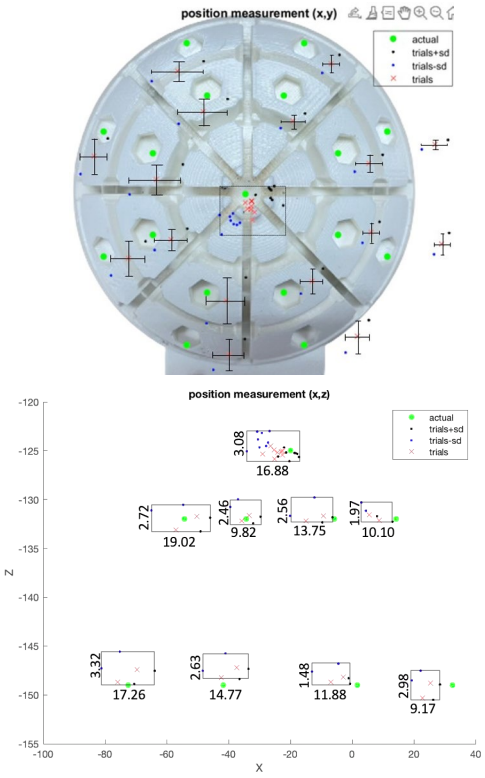

Fig. 12. Position accuracy of the 6-DOF passive robotic arm.

the mapping of the experimental setup, the X-axis has high influence from the first joint of the robotic arm. Therefore, a small miscounting can create noticeable error.

TABLE II. Summary of Position Error

Axis	Error in mm	Error in %
X	18.05	90
Y	27.15	8.23
Z	2.95	2.18

B. *Orientation Accuracy*

The orientation accuracy is shown in Fig. 13 and summarized in Table III. The orientation errors in degrees do

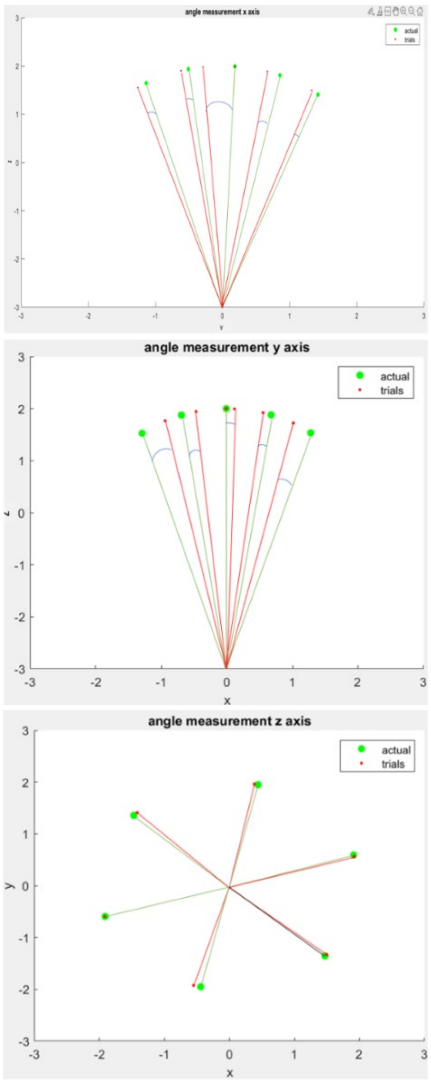

Fig. 13. Orientation accuracy of the 6-DOF passive robotic arm about the X-axis, Y-axis, and Z-axis, respectively.

not show significant difference in all axes. Because of lower resolution and higher noise due to analog output of potentiometers, the fluctuation causing the high error accordingly.

TABLE III. SUMMARY OF ORIENTATION ERROR

Axis	Max error in degrees	Max error in %
X	13.78	22.96
Y	10.23	51.13
Z	8.54	42.72

VI. CONCLUSION

As an alternative strategy, this paper presented a 6-DOF passive robotic arm for the complete tracking of the probe position and orientation. The custom designed handle located at the end effector was assembled from the inner and outer shells, which allows installation of a tiny three-axis force sensor for measuring the probe contact force. The forward kinematics of the robot arm was derived for mapping the joint variables to the position and orientation of the tip. The real-time measurement of the joint angles is achieved from the non-contact magnetic encoders for the first to fourth revolute joints and the rotary potentiometers for the 2-DOF ball joint. The three-dimensional testbed consisting of the radial arrays of hexagonal slots was used for evaluating the position and orientation accuracy of the passive arm. The results of this study can be used as a guideline for further development of passive robotic arms to achieve a higher level of accuracy on tracking the probe trajectory. The simultaneous observation of the ultrasound probe's contacting force, tilting orientation, and operational trajectory in spatial coordinates can provide useful feedback for supporting ultrasonography training.

To enable natural motion of human operators despite the effect of inertia of the robotic arm, the gravity compensation with haptic feedback will be focused in our future study. The passive joints will be replaced by smart servo motors, as used in the custom manipulator [14], to allow torque control with angle feedback. In addition, the validation of accuracy by using the custom test plate designed by considering the anatomical complexity of the abdominal region is essential to apply the results for the actual medical training.

ACKNOWLEDGMENT

This research project is partly supported by Division of Gastroenterology, Department of Medicine, Chulalongkorn University and Tronormos Co., Ltd., Bangkok, Thailand.

REFERENCES

[1] T. Tiyarattanachai, et al., "The feasibility to use artificial intelligence to aid detecting focal liver lesions in real-time ultrasound: a preliminary study based on videos," *Sci. Rep.*, vol. 12, pp. 7749, 2022.

[2] T. Hodges, "Ultrasound probe movement analysis using an inertial measurement unit," M.S. thesis, Department of Mech. Eng., University of Ottawa, 2020.

[3] Z. Jiang, et al., "Automatic normal positioning of robotic ultrasound probe based only on confidence map optimization and force measurement," *IEEE Robot. Autom. Lett.*, vol. 5, no. 2, pp. 1342–1349, 2020.

[4] A. Karamalis, W. Wein, T. Klein, and N. Navab, "Ultrasound confidence maps using random walks," *Med Image Anal.*, vol. 16, no. 6, pp. 1101–1112, 2012.

[5] Y.J. Kim, S. Kim, and J. Choi, "Sarcopenia detection system using RGB-D camera and ultrasound probe: system development and preclinical in-vitro test," *Sensors*, vol. 20, no. 4447, pp. 1–28, 2020.

[6] K. Ito, K. Yodokawa, T. Aoki, J. Ohmiya, and S. Kondo, "A probe-camera system for 3D ultrasound image reconstruction," in *Imaging for Patient-Customized Simulations and Systems for Point-of-Care Ultrasound*, 2017, pp. 129–137.

[7] F. Rousseau, P. Hellier and C. Barillot, "A fully automatic calibration procedure for freehand 3D ultrasound," in *Proc. IEEE Int. Symp. Biomedical Imaging*, 2002, pp. 985–988.

[8] T. Kim, et al., "Versatile low-cost volumetric 3D ultrasound imaging using gimbal-assisted distance sensors and an inertial measurement unit," *Sensors*, vol. 20, no. 6613, pp. 1–15, 2020.

[9] T. Wen, C. Wang, Y. Zhang, and S. Zhou, "A novel ultrasound probe spatial calibration method using a combined phantom and stylus," *Ultrasound Med. Biol.*, vol. 46, no. 8, pp. 2079–2089, 2020.

[10] K. Pornpipatsakul, A. Chenviteesook, and R. Chaichaowarat, "Ultrasound probe movement analysis using depth camera with compact handle design for probe contact force measurement," in *Proc. IEEE/EMBS Annu. Int. Conf.*, 2023.

[11] C. Lugaresi, et al., "MediaPipe: A Framework for building perception pipelines," *arXiv preprint arXiv:1906.08172*, 2019, pp. 1–9.

[12] F. Zhang, et al., "MediaPipe Hands: On-device real-time hand tracking," *arXiv preprint arXiv:2006.10214*, 2020, pp. 1–5.

[13] G. Gao, H. Zhang, X. Wu, and Y. Guo, "Structural parameter identification of articulated arm coordinate measuring machines," *Math. Probl. Eng.*, vol. 2016, no. 4063046, pp. 1–10, 2016.

[14] R. Chaichaowarat, A. Sirichatchaikul, W. Iamkaew, and N. Phondee, "Affordable pipetting robot: gripper design for automatic changing of micropipette and liquid volume control," in *Proc. IEEE/ASME Int. Conf. Advanced Intelligent Mechatronics*, pp. 1275–1280, 2022.